Highly restricted near-surface permafrost extent during the mid-Pliocene warm period

Donglin Guo[1,2*], Huijun Wang[2], Vladimir E. Romanovsky[3,4], Alan M. Haywood[5], Nick Pepin[6], Ulrich Salzmann[7], Jianqi Sun[1], Qing Yan[1], Zhongshi Zhang[8], Xiangyu Li[8], Bette L. Otto-Bliesner[9], Ran Feng[10], Gerrit Lohmann[11], Christian Stepanek[11], Ayako Abe-Ouchi[12], Wing-Le Chan[12], W. Richard Peltier[13], Deepak Chandan[13], Anna S. von der Heydt[14], Camille Contoux[15], Mark A. Chandler[16], Ning Tan[17], Qiong Zhang[18], Stephen J. Hunter[5], Youichi Kamae[19]

[1]*Nansen-Zhu International Research Centre, Institute of Atmospheric Physics, Chinese Academy of Sciences, Beijing, China*

[2]*Key Laboratory of Meteorological Disaster, Ministry of Education/Collaborative Innovation Center on Forecast and Evaluation of Meteorological Disasters, Nanjing University of Information Science & Technology, Nanjing, China*

[3]*Geophysical Institute, University of Alaska Fairbanks, Fairbanks AK 99775 AK, United States of America*

[4]*Earth Cryosphere Institute, Tyumen Scientific Centre SB RAS, Tyumen, Russia*

[5]*School of Earth and Environment, University of Leeds, Woodhouse Lane, Leeds, West Yorkshire, LS29JT, UK*

[6]*School of Environment, Geography and Geosciences, Buckingham Building, Lion Terrace, University of Portsmouth, United Kingdom*

[7]*Department of Geography and Environmental Sciences, Northumbria University, Newcastle upon Tyne NE1 8ST, UK*

[8]*Department of Atmospheric Science, School of Environmental studies, China University of Geoscience, Wuhan 430074, China*

[9]*National Center for Atmospheric Research, Boulder, USA*

[10]*Department of Earth Sciences, University of Connecticut, Storrs, USA*

[11]*Alfred Wegener Institute, Helmholtz Centre for Polar and Marine Research, Bremerhaven, Germany*

[12]*Atmosphere and Ocean Research Institute (AORI), University of Tokyo, Kashiwa, Japan*

[13]*Department of Physics, University of Toronto, Toronto, Canada*

[14]*Institute for Marine and Atmospheric research Utrecht (IMAU), Department of Physics, Utrecht University, Utrecht, The Netherlands.*

[15]*Laboratoire des Sciences du Climat et de l'Environnement, LSCE/IPSL, CEA-CNRS-UVSQ, Université Paris-Saclay, F-91191 Gif-sur-Yvette, France*

[16]*CCSR/GISS, Columbia University, New York, USA*

[17]*Key Laboratory of Cenozoic Geology and Environment, Institute of Geology and Geophysics, Chinese Academy of Sciences, Beijing 100029, China*

[18]*Department of Physical Geography and Bolin Centre for Climate Research, Stockholm University, Stockholm, Sweden*

[19]*Faculty of Life and Environmental Sciences, University of Tsukuba, Tsukuba, 305-8572, Japan*

*Corresponding author. Email: guodl@mail.iap.ac.cn (D. G.)

Abstract

Accurate understanding of permafrost dynamics is critical for evaluating and mitigating impacts that may arise as permafrost degrades in the future; however, existing projections have large uncertainties. Studies of how permafrost responded historically during Earth's past warm periods are helpful in exploring potential future permafrost behavior and to evaluate the uncertainty of future permafrost change projections. Here, we combine a surface frost index model with outputs from the second phase of the Pliocene Model Intercomparison Project to simulate the near-surface (~3–4 m depth) permafrost state in the Northern Hemisphere during the mid-Pliocene warm period (mPWP, ~3.264 to 3.025 Ma). This period shares similarities with the projected future climate. Constrained by proxy-based surface air temperature records, our simulations demonstrate that near-surface permafrost was highly spatially restricted during the mPWP and was 93 ± 3% smaller than the preindustrial extent. Near-surface permafrost was present only in the eastern Siberian uplands, Canadian high Arctic Archipelago and northernmost Greenland. The simulations are similar to near-surface permafrost changes projected for the end of this century under the SSP5-8.5 scenario and provide a perspective on the potential permafrost behavior that may be expected in a warmer world.

Significance statement:

To better understand how near-surface permafrost may respond to future warming, we explore the equilibrium spatial extent of near-surface permafrost during the mid-Pliocene warm period (mPWP), which shares characteristics of the projected future climate. Our simulations, which are constrained by proxy records, suggest highly restricted near-surface permafrost extent during the mPWP, akin to future large-scale permafrost degradation projections of our model for the end of this century. Our study indicates dramatically smaller-than-present near-surface permafrost extent in the geological past under climate conditions analogous to those expected if global warming continues unabated. This will come with critical implications for the global carbon cycle, human livelihoods and infrastructures, and surface and subsurface hydrology.

1. Introduction

Permafrost, that is, ground with a temperature remaining at or below 0 °C for at least two consecutive years (1), currently underlies approximately 22% of the land surface of the Northern Hemisphere (2) and stores approximately 11,000–37,000 km^3 of ground ice (3), 1,330–1,580 Pg of organic carbon (4–5), and a large pool of the harmful substance mercury (6) and various potentially harmful microorganisms (7). Both observations and model simulations indicate that permafrost will likely degrade substantially as global temperature increases (1, 8–9). Any permafrost degradation, accompanied by melting of ground ice and release of organic carbon and harmful substances, will have considerable impacts on ecosystems (10), water resources (11), engineering infrastructure (12–13), climate (4) and human health (7). However, the rate of projected future permafrost decline is subject to large uncertainty due to the variable climate sensitivities of climate models and differences in details of soil-related processes across different models (14–16). Thus, informed policy decisions for mitigation and adaptation are difficult.

Past Earth conditions form a useful laboratory for climate-model verification, as there is no model-independent source of information for future climate, yet model-based projections remain our only quantitative tool for research. Simulation uncertainty can be reduced through comparison of model output against available proxy-based records. To help verify models and evaluate the uncertainty of future permafrost change projections produced with these models, it is necessary to study permafrost during Earth's past (17–20). Of particular interest are past warm periods

92 that share similarities with future conditions.

93 The mid-Pliocene warm period (mPWP: ~3.264 to 3.025 Ma (21)) is the most
94 recent period of sustained (10^4-year timescales) global warmth in geological history
95 (22). It is characterized by land–sea distribution, topography and greenhouse gas
96 levels similar to the present day (21, 23) and arguably represents a natural experiment
97 from which we can gain insights about our future climate (24). Our knowledge of the
98 mPWP has been considerably improved through coordinated model simulations
99 (Pliocene Model Intercomparison Project, PlioMIP) (25–26), together with
100 proxy-based temperature reconstructions (21, 27). PlioMIP Phase 2 (PlioMIP 2)
101 simulations predicted that the global annual mean surface air temperature was 3.2 °C
102 higher in the mPWP than in the preindustrial period (26). In particular, the annual
103 mean mPWP surface air temperature was 7.2 °C higher in arctic regions (28).
104 However, this simulated arctic warming is still weaker than that obtained through
105 proxy-based reconstructions (29).

106 Moreover, simulated winter/summer temperature and precipitation–climate
107 variables, which arguably have the strongest impact on permafrost stability (18, 30),
108 have been shown to be similar for the Mid-Pliocene (3.3–3.0 Ma) and future (as
109 projected for 2100 and 2200 based on the representative concentration pathway (RCP)
110 8.5 scenario) climate for many regions (e.g., parts of the Northern Hemisphere high
111 latitudes) (31). Some of the regions coincide with extensive current presence of
112 permafrost (2). The similarity of both climates suggests that mPWP permafrost state
113 has direct implications for the future permafrost behavior if relict permafrost is not

114 considered. Thus, the study of mPWP permafrost distribution and its associated
115 climate drivers using models and proxy data can improve our understanding of the
116 extent, dynamics and uncertainty of permafrost loss in a warmer future climate.

117 Little is known about the permafrost state in the entire Northern Hemisphere
118 during the mPWP (5), although geological records have been examined to infer the
119 possible formation of permafrost at a few localities during periods approaching the
120 mPWP (32–34). Models can help to derive more spatially resolved information on
121 mPWP permafrost. Here, we use PlioMIP2 climate simulations in combination with a
122 surface frost index (SFI) model (see permafrost diagnosis methods) to examine the
123 spatial pattern of near-surface (~3–4 m depth (35)) permafrost over the entire
124 Northern Hemisphere during the mPWP and compare its extent to that during the
125 preindustrial period. Independent proxy-based temperature data are used as a
126 constraint to evaluate the model-based results.

127 **Results**

128 The multimodel ensemble mean of PlioMIP2 simulations shows that the mean annual
129 surface air temperature is 6.5 ± 2.3 °C higher during the mPWP than during the
130 preindustrial period in present-day permafrost regions (Figure S1). Compared to the
131 preindustrial period, the mean surface air temperature of the warmest month increases
132 by 7.0 ± 3.4 °C, whereas that of the coldest month increases by 5.4 ± 2.5 °C. Twelve
133 out of 17 models indicate a larger increase in the mean surface air temperature of the
134 warmest month than of the coldest month. For the mean winter snow depth, 15 out of

17 models indicate the presence of more snow compared to the preindustrial, with an area-mean increase of 5.5 cm ± 4.1 cm, which is presumably due to warmer air inducing a greater supply of moisture for snowfall (36). Snow acts as a very efficient thermal insulator for the ground during winter, and consequently, it reduces the potential for the presence of permafrost (37–38).

Forced with the PlioMIP2 climate simulations, our permafrost simulations with the SFI model demonstrate that mPWP near-surface permafrost is substantially less extensive than during the preindustrial period (Figure 1B and Figure S2). However, the difference in simulated mPWP near-surface permafrost extent relative to preindustrial shows a wide range (−15% to −96%) across the models, with a multimodel ensemble mean of −77% and a standard deviation of ±24% (Figure 1A). The multimodel ensemble mean indicates that mPWP near-surface permafrost is present only in the eastern Siberian uplands, along the Russian Arctic coast, in the Canadian high Arctic Archipelago, and across northernmost Greenland (Figure 1B).

The percentage difference in mPWP versus preindustrial near-surface permafrost area across models is significantly correlated with the annual mean surface air temperature increase in mPWP versus preindustrial ($R=-0.85$, $P<0.001$) and even more with the temperature increase in the warmest month ($R=-0.90$, $P<0.001$) (Figure S3). The percentage difference in mPWP and preindustrial near-surface permafrost extent is also closely correlated with the equilibrium climate sensitivity (ECS) (Figure S3E, Table S1) of each model ($R=-0.50$, $P<0.05$). Models with higher ECS always simulate greater warming in the present-day permafrost region (Figure S3F), which in

157 turn leads to the simulated absence of mPWP permafrost in those regions.

158 To reduce the large model spread in simulating mPWP permafrost change, we
159 use proxy-based mean annual surface air temperatures at 35 sites (Table S2) to
160 constrain the PlioMIP2 simulations. We classify PlioMIP2 simulations based on an
161 index, the mean bias (MB). The MB is the bias between the simulated and
162 proxy-based surface air temperature anomalies (mPWP minus preindustrial) averaged
163 over the 35 sites (Table S2). It represents the level of agreement between simulations
164 and proxy records in a spatially integrated manner. The MB is exclusively negative for
165 all models but with a wide range from –0.9 °C (EC-Earth3-LR) to –6.6 °C
166 (GISS-E2-1-G) (Figure 2A and Table S1). The models with smaller MB generally
167 have higher spatial correlation coefficients against proxy-based temperature ($R=0.62$,
168 $P<0.01$) (Figure S4, Table S1). According to the MB, the PlioMIP2 simulations can be
169 divided into three groups: (1) –3 °C<MB<0 °C, (2) –5 °C<MB<–3 °C and (3) MB<–
170 5 °C (Figure 2A). Model group 1 has an ensemble mean MB of –1.9 °C, much smaller
171 than those of group 2 (MB: –3.8 °C) and group 3 (MB: –5.7 °C). This finding
172 indicates that model group 1 provides the best level of agreement between simulations
173 and proxy records. Beyond the best fitting model group, basic patterns in the spatial
174 structure of model-data mismatch (individual biases) are also reproduced in the other
175 two groups: at locations of single proxy records, for all three model group ensembles,
176 the bias is mainly negative and generally increases from low to high latitudes (Figure
177 2B–D).

178 The three model groups produce large differences in the ensemble mean extent of

mPWP near-surface permafrost relative to preindustrial extent (Figure 3). Group 1 shows a 93% smaller mPWP near-surface permafrost extent with a very small standard deviation of ±3% across models. In that group, mPWP near-surface permafrost is present mostly in the eastern Siberian uplands, the Canadian high Arctic Archipelago and across northernmost Greenland (Figure 3A). Group 2 exhibits a 69% smaller mPWP near-surface permafrost extent than preindustrial, with a higher standard deviation of ±15% across models. The mPWP near-surface permafrost is present in the Arctic, especially in Canada and western Russia, with much less near-surface permafrost being present in the northern Tibetan Plateau and Alaska (Figure 3B). Group 3 displays a 40% smaller mPWP near-surface permafrost extent than preindustrial, with a standard deviation of ±15% across models. In that group, the absence of mPWP near-surface permafrost relative to the preindustrial period is apparent in southern Alaska and Canada, the northern Western Siberian Plain, and Eastern Siberia/Kamchatka, whereas near-surface permafrost is present in other regions (Figure 3C).

Group 1 models simulate the most realistic surface air temperature change for the mPWP compared to the preindustrial period if the proxy records are taken as a benchmark. By extension, given the close relationship between the simulated permafrost extent and temperature, we consider that the group 1 results, particularly the substantially smaller mPWP near-surface permafrost extent (93 ± 3%), are the most reliable among the PlioMIP2 model ensembles if the state of permafrost is the subject of interest. The 93 ± 3% smaller mPWP near-surface permafrost extent found

201 in group 1 also has a much smaller standard deviation, indicating that the models align
202 well. This result may be related to the uniformly smaller divergence of the group 1
203 models from proxy-based temperature. This smaller mPWP near-surface permafrost
204 extent is associated with an area-averaged 9.6 °C ± 0.6 °C increase in mean annual
205 surface air temperature as well as an area-averaged 5.6 cm ± 4.3 cm increase in mean
206 winter snow depth in present-day permafrost regions during the mPWP relative to the
207 preindustrial period (Figure S5). During the mPWP, near-surface permafrost is found
208 mostly in the eastern Siberian uplands, the Canadian high Arctic Archipelago and
209 across northernmost Greenland. The presence of near-surface permafrost is apparently
210 related to the relatively cool surface air temperature in these regions during the mPWP
211 (Figure S6A), although the temperature has significantly increased compared to that
212 during the preindustrial period (Figure S5A and Figure S6B). Notably, group 1 models
213 still have a substantial cold bias with regard to proxy records in those regions, such as
214 in the eastern Siberian uplands. Thus even the substantially smaller mPWP
215 near-surface permafrost extent relative to the preindustrial period as diagnosed by
216 model group 1 may still slightly underestimate this difference.

217 **Discussion**

218 We discuss here the spatial characteristics of near-surface permafrost during the
219 mPWP based on the PlioMIP2 simulations constrained by proxy-based surface air
220 temperature records, i.e., the results produced by model group 1. For this group of
221 models, mPWP near-surface permafrost is 93 ± 3% less extensive compared to the

preindustrial area. Major areas of simulated mPWP near-surface permafrost are present only in the eastern Siberian uplands, Canadian high Arctic Archipelago and northernmost Greenland.

Our simulations are compared to direct proxy data-based evidence of permafrost distribution. There is proxy data-based evidence for permafrost slightly before and after 3.26–3.0 but none currently reported in the mPWP. The presence of ice wedge casts indicates that permafrost was likely present on Ellesmere Island in Canada's High Arctic during 3.8–3.63 Ma (close to but earlier than the mPWP) (39). The results from some models in group 1 are consistent with this field observation (Figure 3A). It is thought that initial permafrost may have developed in the El'gygytgyn Lake region in northeastern Arctic Russia during the Pliocene Marine Isotope Stage (MIS) M2 cooling events (3.31–3.28 Ma), inferred based on lake sediment records (33, 40). However, the permafrost, formed during MIS M2 cooling, may have thawed in response to significant warming during the mPWP, which followed MIS M2. This appears to be consistent with the simulated absence of permafrost for the respective region as produced by model group 1 (Figure 3A). In addition, permafrost was likely present in the Klondike area in western Canada by approximately 3 Ma (close to but slightly later than the mPWP), indicated by the presence of ice wedge casts (41), consistent with the results from some models in group 1. Moreover, our simulations refine the interpretation from the proxy record in that they suggest that permafrost in the Klondike area may have been only a regional phenomenon (Figure 3A). The absence of permafrost is also inferred from marine fossil sediment records in

244 northwestern Alaska during the Bigbendian marine transgression (slightly after 3 Ma,
245 which is close to but later than the mPWP) (32), in accordance with our results
246 (Figure 3A).

247 Both the magnitude and spatial pattern of the near-surface permafrost extent
248 simulated during the mPWP relative to preindustrial levels, are somewhat similar to
249 the large-scale permafrost degradation projected for the end of the 21st century under
250 the Shared Socioeconomic Pathways (SSP) 5-8.5 scenario (Figure S7C). We selected
251 ten models, based on their success in simulating surface air temperature change during
252 the 20th century (Figure S7A). They project a loss of near-surface permafrost area of
253 77 ± 6% in response to a surface air temperature rise of 7.5 ± 1.1 °C at the end of the
254 21st century under the SSP5-8.5 scenario relative to 1995–2014 (Figure S7B–C), with
255 near-surface permafrost remaining only in the east Siberian uplands, along the
256 Russian Arctic coast and at the Canadian Archipelago (Figure S7C). These findings
257 are in agreement with work presented by Slater and Lawrence (2013) (14) and Koven
258 et al. (2013) (15), who find similar results, with losses of 81 ± 12% and 65% ± 33%,
259 respectively, at the end of the 21st century under the RCP8.5 scenario relative to
260 1986–2005.

261 Notably, all these simulations, including both the future and mPWP, focus on
262 near-surface permafrost only, which appears less resistant to climate warming than
263 deep permafrost (42–43). We also note that a direct comparison between mPWP
264 permafrost extent and future permafrost loss has limitations, as it mixes the effects of
265 greenhouse gas-related warming with those created by differences in topography. The

mPWP simulations are based on a reconstructed paleotopography (21), while projections use present-day topography, and these topographical differences may contribute to the differences in both surface air temperatures and permafrost extent between the two periods. However, if we correct the simulated mPWP climate to account for present-day topography by using the assumed mean atmospheric lapse rate (–0.65 °C/100 m), then we obtain similar results on near-surface permafrost extent with regard to both the smaller extent relative to preindustrial (94 ± 3%) and the spatial pattern of permafrost extent (Figure S8). This finding indicates that localized differences in topography between the mPWP and present day are not a major source of uncertainty in our conclusions.

An additional caveat in the relationship between the mPWP and future permafrost is related to our comparison including the effects of differences in vegetation and surficial geology (e.g., grain size of soil). The mPWP simulations take vegetation change between the mPWP and preindustrial period into account (23, 44), whereas most of the models employed for future projections do not consider vegetation change between the future and present day (45). Exclusion of vegetation change in the models used for future projections could cause polar amplification (associated with greening) to be underestimated (46). Surficial geology has been altered since the mPWP by erosion and land-forming processes that resulted from the sequence of Quaternary glacial-interglacial cycles (47) and thus it could have a different climatic effect during the future compared with the mPWP (48).

Besides, the comparison of permafrost must also acknowledge the effects of the

288 difference between mPWP equilibrium and future SSP transient climate experiments.
289 The SFI model assumes permafrost in equilibrium with a stationary climate, so
290 permafrost may be in an equilibrium state in the mPWP experiment. Although the
291 20-year mean of climate data is used to address the stationarity of climate (14), the
292 timescale may require longer for future permafrost to equilibrate given the thermal
293 resilience of permafrost. Previous speleothem and stratigraphic studies show that even
294 near-surface permafrost persisted, although locally, through past interglacials with
295 multiple millennia of warmer-than-present climate, e.g., the early Holocene (49), MIS
296 5e (50–51) and MIS 11 (52–55). However, despite these intrinsic differences, the
297 mPWP remains one of the best geological analogs for the future due to both general
298 features of Earth surface characteristics and carbon dioxide forcing being comparable
299 to today (26, 31). Consequently, the mPWP provides a laboratory to study the
300 dynamics and extent of permafrost in a warmer-than-present climate that may, in
301 many aspects, be similar to future conditions (31).

302 Based on the success in simulating the present-day permafrost distribution (see
303 evaluation of permafrost diagnosis methods), this study chose the indirect SFI model
304 diagnostic method to investigate the permafrost state during the mPWP, leading to the
305 results discussed above. To assess whether our results depend on the type of
306 permafrost diagnosis method employed, we also consider a direct soil temperature
307 diagnosis. We compare the results derived from the two methods based on climate
308 data and soil temperature data from the same four models (CESM2, CESM1.2,
309 CESM1.0.5, CCSM-UoT) in group 1. These models provide reasonable performance

in capturing the present-day permafrost distribution (Figure S10). When using the direct method, we find that mPWP near-surface permafrost is 86%–99% less extensive than during the preindustrial period (Figure S9A) due to significantly higher mPWP soil temperature, particularly from June to August (Figure S9C). The extent of deeper mPWP permafrost is slightly greater than that of near-surface mPWP permafrost (Figure S9B). The relative difference between mPWP and preindustrial is similar in magnitude to that found when employing the indirect SFI model diagnostic method (mPWP near-surface permafrost extent is 87%–96% smaller than preindustrial for models of group 1) (Table S1), indicating that our results are not highly dependent on the permafrost diagnostic method.

Uncertainties in our SFI simulations are mostly caused by uncertainties in model boundary conditions (21) and uncertainties in model physics (26). Furthermore, the coarse resolution of some of the climate models used (e.g., NorESM1-L, 3.75° ×3.75°) provides less regional detail, and limits particularly the ability to produce realistic and detailed climatic conditions at the edges of permafrost regions. An additional source of uncertainty is related to the poor data coverage in some high latitude regions and uncertainty ranges of proxy data-based temperature estimates. However, as the majority (n=21) of our selected paleo-sites are located north of 50°N and the overall uncertainty ranges of temperature estimates are below ±2 °C (Table S2), it is unlikely that data uncertainties have a major impact on the ranking order of our three model groups (Figure 2) (see proxy data-based surface air temperature data).

The indirect SFI model diagnostic method does not consider vegetation, organic

matter and excess ground ice in surface/subsurface characteristics. Increases in vegetation cover and height generally warm soil by increasing snow depth in winter, and cool soil by increasing evapotranspiration and surface shading in summer (37, 56–57). Soil organic matter can reduce the annual mean soil temperature and decrease the active layer thickness (42, 58). Excess ground ice can retard the thawing of near-surface permafrost due to latent heat effects (16, 38, 59). However, given the lack of sufficiently detailed information on the surface and soil characteristics of the mPWP, it is not yet possible to robustly examine these impacts. More work needs to quantify the distribution of mPWP vegetation and other permafrost-relevant land surface conditions, further exploring their impact on the simulation of near-surface permafrost during the mPWP.

Despite these uncertainties, our work provides an important step in characterizing the extent of mPWP permafrost and relating its spatial distribution to climatic and permafrost changes that are expected for the coming decades to centuries based on projections of future climate. Beyond providing a quantitative and self-consistent analysis of mPWP permafrost in comparison to today based on the newest PlioMIP2 model output, our work also allows verification of permafrost simulations by means of model-independent proxy records. We illustrate links between mPWP and potential future climate based on similarities of both climate states, indicating that mPWP permafrost has direct implications for the state and stability of future permafrost. Based on our findings, the future of Northern Hemisphere near-surface permafrost appears bleak. Continued climate warming and

related near-surface permafrost degradation may cause changes in ambient and environmental conditions (7, 11, 13, 60–61) that humans have not yet experienced, implying an imperative to further highlight the importance of permafrost degradation. Consequently, our study shows that the response of permafrost to past sustained warmth is valuable for understanding of permafrost degradation and associated climate, ecological, and societal impacts in our warming world.

Methods

mPWP and preindustrial climate simulation data for permafrost simulation

mPWP and preindustrial climate data were obtained from 16 coupled atmosphere-ocean climate models (AOGCM) in the Pliocene Model Intercomparison Project Phase 2 (PlioMIP2) (26) and an atmosphere-only climate model (AGCM) from Yan et al. (2016) (62). Key details of these models are shown in Table S1. All 17 models provide monthly surface air temperature (2 m) and precipitation (used to calculate snow depth). These data are employed to drive the SFI model, with a snow density assumption of 250 kg m^{-3} according to Slater and Lawrence (2013) (14). For 8 of the 17 models (CESM2, CESM1.2, CESM1.0.5, CCSM4, CCSM-UoT, EC-Earth3-LR, GISS-E2-1-G, IPSLCM6A-LR), monthly soil temperatures were available and used to directly diagnose permafrost distribution (the SFI model was not used in this case). In addition, monthly snow depth and snow mass (used to calculate snow density) were also available for CESM2 and were used to drive the SFI model in combination with monthly surface air temperature. Compared to PlioMIP1, PlioMIP2

simulations are underpinned by state-of-the-art boundary conditions (e.g., new paleogeographic reconstructions detailing ocean bathymetry, land ice surface topography, and updated Pliocene soil and lake distribution data sets) from the latest Pliocene Research-Interpretation and Synoptic Mapping (PRISM) version 4 (21). Sea ice is predicted dynamically by the climate models. The Arctic is nearly sea ice free in summer but covered by substantial amounts of sea ice in winter during the mPWP as indicated by the majority of the models (28). Additional details regarding the mPWP simulation setup can be found in Haywood et al. (2016) (23). All but two of the AOGCMs have produced simulations with a length in excess of 1,000 model years for both mPWP and preindustrial experiments (26). The final 100 years of each simulation are analyzed in this study. In the case of the AGCM, the simulation ran for a length of 10 (7) years for mPWP (preindustrial), respectively (62), and the final 5 years of results are analyzed. Data for the models CESM2, EC-Earth3-LR, GISS-E2-1-G, IPSL-CM6A-LR and NorESM1-F are archived at the Earth System Grid Federation (ESGF) gateway (https://esgf-node.llnl.gov/). Data from other models have been provided by the corresponding modeling groups (26, 62).

CRU climate data

Observed monthly surface air temperature and precipitation (used to calculate snow depth) are obtained from CRU TS 4.04 data at a spatial resolution of 0.5° × 0.5° available at https://crudata.uea.ac.uk/cru/data/hrg/cru_ts_4.04/. These data are used to drive the SFI model to diagnose preindustrial permafrost and to correct simulated climate data from PlioMIP2. The data set covers the time period of 1901–2019. In the

absence of CRU TS 4.04 data for 1850, we used the years 1901–1930 to represent the preindustrial period. This choice is justified because the state of the climate does not substantially change over these periods (63). CRU TS 4.04 is a gridded data set that is produced from station observations. Station anomalies are first interpolated to a high-resolution grid and then added to an existing climatology to yield absolute values. More details can be found in Harris et al. (2020) (64). CRU is an established data set and has been used worldwide for research on climate change detection (65–67).

International Permafrost Association map

The International Permafrost Association (IPA) map (68) is used as a source of observations to validate our permafrost simulations for the preindustrial period. Because the map is produced using data from 1960–1993 (68) while the preindustrial period refers to 1850, there is an unavoidable period mismatch in this validation. However, at least in Eastern Siberia, the time range from 1901 to 1960 does not appear to be an example of continuous permafrost degradation but rather was characterized by intermittent periods of increases and reductions in active layer thickness (69). This finding provides some confidence that the IPA map may be suitable to provide estimates of large-scale patterns of permafrost as present during the earlier part of the 20th century and, by extension, during the preindustrial period. The map discriminates permafrost into continuous, discontinuous, sporadic and isolated types. Given that the simulation at a resolution of 0.5° × 0.5° may identify only continuous and discontinuous permafrost (16), we limited the validation of our simulations to areas of continuous and discontinuous permafrost. The permafrost data

are available at https://nsidc.org/data/GGD318/versions/2 and are considered to be one of the best available sources on permafrost distribution (14).

Proxy data-based surface air temperature data

We used quantitative climate estimates from the late Pliocene (~3.6 to 2.6 Ma) paleobotanical data set (44), which has been updated for assessing model experiments of the PlioMIP2 (29). Updates refer to additional quantitative climate estimates and uncertainty assessments, including confidence levels for each site. To reduce the risk of a potential methodological bias, we used Late Pliocene temperature estimates that were derived from the paleobotanical record (i.e., fossil pollen, leaves, wood) using a range of different quantitative and semiquantitative methods, including bioclimatic ranges of nearest living relatives, oxygen isotopes of fossil wood or the physiognomy of fossil leaves. The uncertainty is provided for each mean annual temperature estimate (Table S2). Temperature estimates based on nearest living relative approaches generally include a bioclimatic range in which all taxa of the reconstructed paleovegetation can coexist. In addition, we also provide, where available, the temporal variability, which indicates the variability in the reconstructed temperature over the time period covered by the fossil record (e.g., orbitally controlled cold and warm cycles). Qualitative confidence (very high, high, medium, and low) of temperature estimates at each site is assessed based on (a) age control, (b) resolution, (c) fossil preservation and (d) the estimation method, whereby age control and estimation method were treated as the most important criteria (Table S2) (29). Although estimates with a high confidence level might be more reliable than those

441 with lower confidence, differences in confidence level appear to have a rather low
442 impact on our data-model comparison. There is good consistency between
443 temperature estimates derived from high- versus lower-confidence sites, particularly
444 in high-latitude Northeast Asia and North America (29).

445 Proxy-based mean annual surface air temperature data from 35 sites were
446 selected for this study to constrain the PlioMIP2 simulations. Key details of these sites
447 are shown in Table S2. Site choices exclude (1) sites with modern altitudes above
448 1000 m due to large uncertainties in estimating Pliocene paleo-altitudes, (2) marine
449 sites, and (3) tropical terrestrial sites with latitudes below 20°N (near the southern
450 limit of Northern Hemisphere permafrost) due to their small representation within the
451 permafrost region in the Northern Hemisphere. The selected sites show good spatial
452 coverage across latitudes (Figure 2), allowing a comprehensive data-model
453 comparison. Data coverage is poor in the high latitudes of Western Siberia, eastern
454 Scandinavia and the boreal zone of central North America. However, the majority
455 (n=21) of our selected sites are located north of 50°N, providing a good benchmark
456 for evaluating the ability of climate models to simulate high-latitude climates in the
457 permafrost zone.

458 We use the temperature midpoints of our proxy estimates as a benchmark to test
459 the PlioMIP2 model performance and then rank the model according to the mean bias
460 (MB), assuming that the distribution of possible temperature values is concentrated
461 near the center of the temporal and bioclimatic ranges (e.g., assuming a normal
462 distribution) (29). All the models consistently show a cold MB, with the least cold

463 MB being –0.9 °C for EC-Earth3-LR (Figure 2, Table S1). Moreover, most of the data
464 uncertainty ranges are below ±2.0 °C (Table S2). Therefore, it appears unlikely that
465 the uncertainty ranges profoundly affect the ranking order of our 3 model groups
466 (Figure 2). However, the uncertainty could alter the thresholds of the classification
467 (i.e., 0 °C, –3 °C and –5 °C for the midpoints of our proxy estimates). Proxy-based
468 temperature anomalies are calculated as individual site records minus the nearest grid
469 cell-mean CRU surface air temperature during 1901–1930, while the simulated
470 temperature anomaly is calculated as mPWP minus preindustrial temperature at any
471 model grid cell.

472 Our proxy data-model comparison is based on comparing simulated grid
473 cell-mean surface air temperature anomalies with individual site proxy-based surface
474 air temperature anomalies; thus, it includes a scale mismatch. This mismatch may
475 cause uncertainties, especially in areas of complex relief. However, such uncertainties
476 are considered to be small in this study. Most of our paleobotanical sites have
477 elevations below 350 m, and sites that today are located above 1000 m are explicitly
478 excluded from the data-model comparison. In addition, the majority of our
479 temperature estimates have been derived from palynological records that reflect
480 pollen influx from the regional dominant vegetation communities. Consequently, the
481 respective temperature estimates relate to a wider catchment area than the specific
482 proxy location. Therefore, reconstructed temperatures are representative of a high
483 proportion of the simulated grid cell (29). Beyond our study, these proxy temperature
484 records have already been used to evaluate the ability of models from the PlioMIP1 to

485 simulate climate during the mPWP (29).

486 **Permafrost diagnosis methods**

487 Two methods were used to diagnose permafrost: (1) the indirect permafrost model
488 method and (2) the direct AOGCM-modeled soil temperature method.

489 For the indirect permafrost model diagnostic method, the surface frost index (SFI)
490 model was used to estimate the near-surface permafrost extent (70):

491 $$\mathrm{SFI} = \frac{\sqrt{DDF^*}}{\sqrt{DDF^*}+\sqrt{DDT}} \quad (1)$$

492 where DDF is the sum of freezing degree days. The label "*" denotes an
493 incorporation of snow insulation effects that results in a decrease in the DDF
494 (70). DDT is the sum of thawing degree days. For specific equations, see the
495 supplementary information (Equation set for the SFI model). The SFI values vary
496 from 0 to 1. If SFI>0.6, then either discontinuous or continuous permafrost was
497 assumed. Model input requires four climate elements: surface air temperature in the
498 warmest and coldest months as well as mean winter snow depth and snow density (the
499 latter two to incorporate snow insulation effects). Surface air temperatures in the
500 warmest and coldest months were derived from simulated monthly surface air
501 temperature data. The mean winter snow depth is calculated using monthly
502 precipitation (see below), and the mean winter snow density is fixed at 250 kg m^{-3}
503 (14).

504 The mean winter snow depth was calculated as (70)

505 $$\bar{Z}_s = sin^2\,\emptyset\,\{\sum_{i=1}^{k}[(P_i/\rho_r)(k-(i-1))]/k\,\} \quad (2)$$

506 where $\bar{Z}_s$ is the mean winter snow depth and P_i is the precipitation in the i_{th} month

507 (i=1, 2,…, k) when the mean surface air temperature is ≤ 0 °C. ρ_r is snow density
508 (250 kg m^{-3} (14)). $\emptyset$ is the latitude. This method weights snowfall by the time of its
509 occurrence (earlier winter snowfall has greater weighting than later spring snowfall)
510 and considers the fact that the magnitude and duration of snow thaw varies with solar
511 forcing (which is dependent on latitude).

512 The SFI model represents the importance of temperature in permafrost formation
513 and considers any snow insulation effect but does not use information about the
514 surface state (topography, vegetation, etc.). It indicates sustainability of the upper
515 (near-surface, ~3–4 m depth (35)) permafrost layer under stationary climate
516 conditions. While climate stationarity is implicitly assumed, it is appropriate for this
517 study to examine the permafrost state in two stabilized scenarios: the mPWP and the
518 preindustrial. The SFI model requires readily available input climate data and is
519 characterized by ease of application and rapid computation, allowing us to explore
520 permafrost change at various temporal and spatial scales. Slater and Lawrence (2013)
521 indicated that more information regarding permafrost change can be provided by the
522 SFI model than is available via raw diagnostics using soil temperature from climate
523 models (14).

524 For the direct AOGCM-modeled soil temperature diagnostic method, the
525 following assumption is made: if there is at least one near-surface soil layer in which
526 the monthly soil temperature remains below 0 °C for 24 consecutive months, then the
527 respective grid cell is identified as containing near-surface permafrost (71–74). This
528 method is used for CESM2, CESM1.2, CESM1.0.5, CCSM4, CCSM-UoT and

IPSLCM6A-LR because soil temperatures are available for these models. Although soil temperatures for EC-Earth3-LR and GISS-E2-1-G are also available, we excluded them from our analyses due to a shallow soil column (<3.0 m). All soil temperature data were interpolated to a common horizontal resolution of 0.9° × 1.25° and to a vertical resolution of 0.1 m for comparison.

Evaluation of permafrost diagnosis methods

To decrease uncertainties in permafrost simulations, the two aforementioned permafrost diagnosis methods were evaluated based on the IPA map to select the optimal method for the present study. Based on the direct soil temperature method (raw AOGCM), CESM2, CESM1.2, CESM1.0.5, CCSM4 and CCSM-UoT show similar absolute biases, apparently smaller than that of IPSLCM6A-LR (Figure S10). Since only CESM2 provides snow depth and snow mass data, it is used to further evaluate the diagnosis methods. The absolute bias of CESM2 using soil temperatures (Figure S11A) is larger than that using the indirect SFI diagnostic method driven by (1) CESM2 surface air temperature and direct snow depth/mass (Figure S11B), (2) CESM2 surface air temperature and precipitation-calculated snow depth (Figure S11C), and (3) coarse resolution CRU surface air temperature and precipitation-calculated snow depth (resampled to CESM grid cell, 0.9° × 1.25°) (Figure S11D). This finding indicates that the indirect SFI model can capture the present-day permafrost distribution more reasonably than direct soil temperatures. The coarse-resolution CRU surface air temperature and precipitation-calculated snow depth yield the least absolute bias (Figure S11B–D). In addition, high-resolution (0.5°

551 × 0.5°) CRU surface air temperature and precipitation-calculated snow depth-based
552 results provide more regional details (Figure S12), although the derived permafrost
553 area has a somewhat larger absolute bias (5.2×10^6 km^2) (Figure S12) than that based
554 on the coarse-resolution (CESM grid cell) method (4.6×10^6 km^2) (Figure S11D).

555 As shown in Figure S12, the permafrost extent computed based on the
556 high-resolution CRU surface air temperature and precipitation-calculated snow depth
557 broadly resembles the IPA map, despite an overestimation in the Labradorean region
558 in northeastern Canada and on the eastern Tibetan Plateau, and a slight
559 underestimation in southern Alaska and in the northern part of the Western Siberian
560 Plain. Based on this sensitivity analysis, our study employs the indirect SFI model
561 method driven by high-resolution CRU surface air temperature and
562 precipitation-calculated snow depth to obtain near-surface permafrost distribution
563 during the preindustrial period.

564 **Simulation of near-surface permafrost during the mPWP**

565 For the mPWP permafrost simulation, we first correct systematic biases in the
566 simulated mPWP climate data using the anomaly method. Specifically, the simulated
567 mPWP climate anomaly is added to the present-day observed climatology, i.e.,
568 high-resolution CRU climatology (1901–1930). The anomaly of surface air
569 temperature denotes the absolute temperature change between the mPWP and
570 preindustrial period, while the anomaly of snow depth denotes a percentage change in
571 snow depth. Then, the corrected climate data are used to drive the SFI model to obtain
572 the permafrost distribution during the mPWP. For comparison, we also analyze the

573 mPWP permafrost distribution obtained with the SFI model driven by raw climate
574 data (i.e., without correcting any systematic biases) from the three model groups
575 (Figure S13). The permafrost distributions based on raw climate data are similar
576 overall to those based on corrected climate data (Figure S13 and Figure 3).
577 Simulations based on raw climate data illustrate slightly smaller permafrost extent
578 during the mPWP than those based on corrected climate data. In addition, raw climate
579 data appear to simulate a larger mPWP permafrost extent in Canada and the Tibetan
580 Plateau but a smaller extent in Russia (Figure S13). This finding corresponds to cooler
581 temperatures in Canada and the Tibetan Plateau and warmer temperatures in Russia
582 (eastern Siberian uplands) in raw climate data (Figure S14) relative to corrected data
583 (Figure S6).

584 **Permafrost projection method**

585 We use simulated historical (1901–2014) and future (2015–2100, SSP5-8.5 scenario)
586 climate data from 22 models participating in the sixth phase of the Coupled Model
587 Intercomparison Project (CMIP6). The climate data sets provided by all models
588 include monthly surface air temperature and precipitation (used to calculate snow
589 depth). The characteristics of the CMIP6 models considered here are shown in Table
590 S3 together with basic model-derived temperature and permafrost statistics. Details
591 regarding the design of the CMIP6 simulations can be found in Eyring et al. (2016)
592 (45). The climate model data sets employed here have been retrieved from the ESGF
593 (https://esgf-node.llnl.gov/).

594 Similar to the mPWP permafrost simulation, we use the anomaly method to

correct systematic biases in simulated historical and future climate data. The anomaly of each simulated climate variable is first calculated relative to the period of 1995–2014 and then added to the present-day (1995–2014) high-resolution CRU climatology to derive the climate forcing for the permafrost simulation. Given the implicit assumption of climatic stationarity in the SFI model, corrected climate data are averaged using a 20-year sliding window (14). Near-surface permafrost distributions for both the end of the 21st century and the present-day are simulated using the SFI model, which is driven by the 20-year averages of corrected climate data over the periods of 2080–2099 and 1995–2014, respectively. The difference between the two simulated permafrost distributions indicates future the change in near-surface permafrost during the end of the 21st century relative to the present day.

In addition, we constrain the 22 CMIP6 models for the present day using the mean bias (MB) between the simulated and CRU surface air temperature anomalies (1995–2014 minus 1901–1930) averaged over the present-day permafrost region. As a result, 10 preferred models are chosen due to their small MBs (–0.3 °C<MB<0.3 °C) (Figure S7A, Table S3). The permafrost projections produced by these 10 preferred models are the focus of most of the analyses of present-day/future permafrost changes (Figure S7).

References

1. B. Biskaborn *et al.*, Permafrost is warming at a global scale. *Nat. Commun.* **10**,

264 (2019).

2. J. Obu *et al.*, Northern Hemisphere permafrost map based on TTOP modelling for 2000–2016 at 1 km^2 scale. *Earth Sci. Rev.* **193**, 299–316 (2019).

3. T. Zhang, R. Barry, K. Knowles, J. Heginbottom, J. Brown, Statistics and characteristic of permafrost and ground-ice distribution in the Northern Hemisphere. *Polar Geogr.* **31**, 47–68 (2008).

4. E. Schuur *et al.*, Climate change and the permafrost carbon feedback. *Nature* **520**, 171–179 (2015).

5. K. Miner *et al.*, Permafrost carbon emissions in a changing Arctic. *Nat. Rev. Earth Environ.* **3**, 55–67 (2022).

6. P. Schuster *et al.*, Permafrost stores a globally significant amount of mercury. *Geophys. Res. Lett.* **45**, 1463–1471 (2018).

7. V. D'Costa *et al.*, Antibiotic resistance is ancient. *Nature* **477**, 457–461 (2011).

8. J. Aalto, S. Harrison, M. Luoto, Statistical modelling predicts almost complete loss of major periglacial processes in Northern Europe by 2100. *Nat. Commun.* **8**, 515 (2017).

9. S. Chadburn *et al.*, An observation-based constraint on permafrost loss as a function of global warming. *Nat. Clim. Change* **7**, 340–344 (2017).

10. J. Vonk *et al.*, Reviews and syntheses: effects of permafrost thaw on Arctic aquatic ecosystems. *Biogeosci.* **12**, 7129–7167 (2015).

11. A. Liljedahl *et al.*, Pan-Arctic ice-wedge degradation in warming permafrost and its influence on tundra hydrology. *Nat. Geosci.* **9**, 312–318 (2016).

637 12. J. Hjort *et al.*, Degrading permafrost puts Arctic infrastructure at risk by
638 midcentury. *Nat. Commun.* **9**, 5147 (2018).
639 13. J. Hjort *et al.*, Impacts of permafrost degradation on infrastructure. *Nat. Rev.*
640 *Earth Environ.* **3**, 24–38 (2022).
641 14. A. Slater, D. Lawrence, Diagnosing present and future permafrost from climate
642 models. *J. Clim.* **26**, 5608–5623 (2013).
643 15. C. Koven, W. Riley, A. Stern, Analysis of permafrost thermal dynamics and
644 response to climate change in the CMIP5 Earth System Models. *J. Clim.* **26**,
645 1877–1900 (2013).
646 16. C. Burn, F. Nelson, Comment on "A projection of severe near-surface permafrost
647 degradation during the 21st century" by David M. Lawrence and Andrew G. Slater.
648 *Geophys. Res. Lett.* **33**, L21503 (2006).
649 17. J. Tierney *et al.*, Past climates inform our future. *Science* **370**, eaay3701 (2020).
650 18. S. Smith, H. O'Neill, K. Isaksen, J. Noetzli, V. Romanovsky, The changing
651 thermal state of permafrost. *Nat. Rev. Earth Environ.* **3**, 10–23 (2022).
652 19. K. Saito *et al.*, LGM permafrost distribution: how well can the latest PMIP
653 multi-model ensembles perform reconstruction? *Clim. Past* **9**, 1697–1714 (2013).
654 20. Y. Liu, D. Jiang, Mid-Holocene permafrost: Results from CMIP5 simulations. *J.*
655 *Geophys. Res. Atmos.* **121**, 221–240 (2016).
656 21. H. Dowsett *et al.*, The PRISM4 (mid-Piacenzian) paleoenvironmental
657 reconstruction. *Clim. Past* **12**, 1519–1538 (2016).
658 22. A. Haywood, H. Dowsett, A. Dolan, Integrating geological archives and climate

659 models for the mid-Pliocene warm period. *Nat. Commun.* **7**, 10646 (2016).
660 23. A. Haywood *et al.*, The Pliocene Model Intercomparison Project (PlioMIP) Phase
661 2: scientific objectives and experimental design. *Clim. Past* **12**, 663–675 (2016).
662 24. H. Dowsett *et al.*, Sea surface temperature of the mid-Piacenzian ocean: A
663 Data-Model Comparison. *Sci. Rep.* **3**, 2013 (2013).
664 25. A. Haywood *et al.*, Large-scale features of Pliocene climate: Results from the
665 Pliocene Model Intercomparison Project. *Clim. Past* **9**, 191–209 (2013).
666 26. A. Haywood *et al.*, The Pliocene Model Intercomparison Project Phase 2:
667 large-scale climate features and climate sensitivity. *Clim. Past* **16**, 2095–2123
668 (2020).
669 27. H. Dowsett *et al.*, Joint investigations of the Middle Pliocene climate I: PRISM
670 paleoenvironmental reconstructions. *Glob. Planet. Change* **9**, 169–195 (1994).
671 28. W. de Nooijer *et al.*, Evaluation of Arctic warming in mid-Pliocene climate
672 simulations. *Clim. Past* **16**, 2325–2341 (2020).
673 29. U. Salzmann *et al.*, Challenges in quantifying Pliocene terrestrial warming
674 revealed by data–model discord. *Nat. Clim. Change* **3**, 969–974 (2013).
675 30. D. Guo, J. Sun, H. Li, T. Zhang, V. Romanovsky, Attribution of historical
676 near-surface permafrost degradation to anthropogenic greenhouse gas warming.
677 *Environ. Res. Lett.* **15**, 084040 (2020).
678 31. K. Burke *et al.*, Pliocene and Eocene provide best analogs for near future climates.
679 *Proc. Nat. Acad. Sci.* **115**, 13288–13293 (2018).
680 32. L. Carter, J. Brigham-Grette, L. Marincovich, V. Jr Pease, J. Hillhouse, Late

681 Cenozoic Arctic Ocean sea ice and terrestrial paleoclimate. *Geology* **14**, 675–678
682 (1986).
683 33. V. Wennrich *et al.*, Impact processes, permafrost dynamics, and climate and
684 environmental variability in the terrestrial Arctic as inferred from the unique 3.6
685 Myr record of Lake El'gygytgyn, Far East Russia-A review. *Quaternary Sci. Rev.*
686 **147**, 221–244 (2016).
687 34. J. Murton, What and where are periglacial landscapes? *Permafrost Periglac.*
688 *Process.* **32**, 186–212 (2021).
689 35. IPCC, Summary for Policymakers. In: *IPCC Special Report on the Ocean and*
690 *Cryosphere in a Changing Climate* [H. Pörtner *et al.* (eds.)]. Cambridge
691 University Press, Cambridge, UK and New York, NY, USA, pp. 3–35 (2019).
692 36. X. Zhong *et al.*, Spatiotemporal variability of snow depth across the Eurasian
693 continent from 1966 to 2012. *The Cryosphere* **12**, 227–245 (2018).
694 37. F. Domine, K. Fourteau, G. Picard, G. Lackner, D. Sarrazin, M Poirier,
695 Permafrost cooled in winter by thermal bridging through snow-covered shrub
696 branches. *Nat. Geosci.* **15**, 554–560 (2022).
697 38. L. Farquharson, V. Romanovsky, A. Kholodov, D. Nicolsky, Sub-aerial talik
698 formation observed across the discontinuous permafrost zone of Alaska. *Nat.*
699 *Geosci.* **15**, 475–481 (2022).
700 39. N. Rybczynski, J. Gosse, C. Harington, R. Wogelius, A. Hidy, M. Buckley,
701 Mid-Pliocene warm-period deposits in the High Arctic yield insight into camel
702 evolution. *Nature Commun.* **4**,1550 (2013).

703 40. V. Wennrich *et al.*, Pliocene to Pleistocene climate and environmental history of
704 Lake El'gygytgyn, Far East Russian Arctic, based on high-resolution inorganic
705 geochemistry data. *Clim. Past*, **10**, 1381–1399 (2014).
706 41. D. Froese, R. Barendregt, R. Enkin, J. Baker, Paleomagnetic evidence for
707 multiple Late Pliocene–Early Pleistocene glaciations in the Klondike area, Yukon
708 Territory. *Can. J. Earth Sci.* **37**, 863–877 (2000).
709 42. D. Lawrence, A. Slater, V. Romanovsky, D. Nicolsky, Sensitivity of a model
710 projection of near-surface permafrost degradation to soil column depth and
711 representation of soil organic matter. *J. Geophys. Res.* **113**, F02011 (2008).
712 43. D. Nicolsky, V. Romanovsky, Modeling long-term permafrost degradation. *J.*
713 *Geophys. Res. Earth Surface* **123**, 1756–1771 (2018).
714 44. U. Salzmann, A. Haywood, D. Lunt, P. Valdes, D. Hill, A new global biome
715 reconstruction and data-model comparison for the Middle Pliocene. *Global Ecol.*
716 *Biogeogr*. **17**, 432–447 (2008).
717 45. V. Eyring *et al.*, Overview of the Coupled Model Intercomparison Project Phase 6
718 (CMIP6) experimental design and organization. *Geosci. Model Dev.* **9**, 1937–
719 1958 (2016).
720 46. R. O'ishi, A. Abe-Ouchi, Influence of dynamic vegetation on climate change
721 arising from increasing CO_2. *Clim. Dyn.* **33**, 645–663 (2009).
722 47. C. Batchelor *et al.*, The configuration of Northern Hemisphere ice sheets through
723 the Quaternary. *Nat Commun.* **10**, 3713 (2019).
724 48. M. Pound, J. Tindall, S. Pickering, A. Haywood, H. Dowsett, U. Salzmann, Late

725 Pliocene lakes and soils: a global data set for the analysis of climate feedbacks in
726 a warmer world. *Clim. Past* **10**, 167–180 (2014).
727 49. C. Burn, Cryostratigraphy, paleogeography, and climate change during the early
728 Holocene warm interval, western Arctic coast, Canada. *Can. J. Earth Sci.*
729 **34**, 912–925 (1997).
730 50. A. Reyes, D. Froese, B. Jensen, Permafrost response to last interglacial warming:
731 field evidence from non-glaciated Yukon and Alaska. *Quaternary Sci. Rev.* **29**,
732 3256–3274 (2010).
733 51. K. Ashastina, L. Schirrmeister, M. Fuchs, F. Kienast, Palaeoclimate
734 characteristics in interior Siberia of MIS 6-2: First insights from the Batagay
735 permafrost mega-thaw slump in the Yana Highlands. *Clim. Past* **13**, 795–818
736 (2017).
737 52. D. Froese, J. Westgate, A. Reyes, R. Enkin, S. Preece, Ancient Permafrost and a
738 Future, Warmer Arctic. *Science* **321**, 1648 (2008).
739 53. N. Biller-Celander *et al.*, Increasing Pleistocene permafrost persistence and
740 carbon cycle conundrums inferred from Canadian speleothems. *Sci. Adv.* **7**,
741 eabe5799 (2021).
742 54. J. Murton *et al.*, A multimethod dating study of ancient permafrost, Batagay
743 megaslump, east Siberia. *Quaternary Res.* **105**, 1–22. (2022).
744 55. A. Vaks et al., Palaeoclimate evidence of vulnerable permafrost during times of
745 low sea ice. *Nature* **577**, 221–225 (2020).
746 56. M. Heijmans *et al.*, Tundra vegetation change and impacts on permafrost. *Nat.*

747 *Rev. Earth Environ.* **3**, 68–84 (2022).
748 57. M. Sturm *et al.*, Winter biological processes could help convert arctic tundra to
749 shrubland. *Bioscience* **55**, 17–26 (2005).
750 58. D. Nicolsky, V. Romanovsky, V. Alexeev, D. Lawrence, Improved modeling of
751 permafrost dynamics in a GCM land-surface scheme. *Geophys. Res. Lett.* **34**,
752 L08501 (2007).
753 59. H. Lee, S. Swenson, A. Slater, D. Lawrence, Effects of excess ground ice on
754 projections of permafrost in a warming climate. *Environ. Res. Lett.* **9**, 124006
755 (2014).
756 60. G. Hugelius *et al.*, Estimated stocks of circumpolar permafrost carbon with
757 quantified uncertainty ranges and identified data gaps. *Biogeosci.* **11**, 6573–6593
758 (2014).
759 61. F. Cheng *et al.*, Alpine permafrost could account for a quarter of thawed carbon
760 based on Plio-Pleistocene paleoclimate analogue. *Nat. Commun.* **13**, 1329 (2022).
761 62. Q. Yan *et al.*, Enhanced intensity of global tropical cyclones during the
762 Mid-Pliocene warm period. *Proc. Nat. Acad. Sci.* **113**, 12963–12967 (2016).
763 63. IPCC. Summary for Policymakers. In: *Climate Change 2021: The Physical*
764 *Science Basis. Contribution of Working Group I to the Sixth Assessment Report of*
765 *the Intergovernmental Panel on Climate Change* [V. Masson-Delmotte et al.
766 (eds.)]. Cambridge University Press (2021).
767 64. I. Harris *et al.*, Version 4 of the CRU TS monthly high-resolution gridded
768 multivariate climate dataset. *Sci. Data* **7**, 109 (2020).

769 65. K. Trenberth *et al.*, Global warming and changes in drought. *Nat. Clim. Change* **4**,
770 17– 22 (2014).
771 66. Y. Zhu, A tripole winter precipitation change pattern around the Tibetan Plateau
772 in the late 1990s. *Atmos. Ocean. Sci. Lett.* **15**, 100223 (2022).
773 67. D. Chen, Y. Gao, Y. Zhang, T. Wang, Effects of spring Arctic sea ice on summer
774 drought in the middle and high latitudes of Asia. *Atmos. Ocean. Sci. Lett.* **15**,
775 100138 (2022).
776 68. J. Brown, O. Jr, J. Heginbottom, E. Melnikov, Circum-arctic map of permafrost
777 and ground-ice conditions, Resources, Circum-Pacific Map Series CP-45, scale
778 1:10,000,000, 1 sheet (1997).
779 69. T. Sazonova, V. Romanovsky, J. Walsh, D. Sergueev, Permafrost dynamics in the
780 20^{th} and 21^{st} centuries along the East Siberian transect. *J. Geophys. Res.* **109**,
781 D01108 (2004).
782 70. F. Nelson, S. Outcalt, A computational method for prediction and regionalization
783 of permafrost. *Arct. Alp. Res.* **19**, 279–88 (1987).
784 71. R. Li *et al.*, Simulated response of the active layer thickness of permafrost to
785 climate change. *Atmos. Ocean. Sci. Lett.* **14**, 100007 (2021).
786 72. D. Guo, H. Wang, Simulation of permafrost and seasonally frozen ground
787 conditions on the Tibetan Plateau, 1981-2010. *J. Geophys. Res. Atmos.* **118**,
788 5216–5230 (2013).
789 73. D. Guo, H. Wang, D. Li, A projection of permafrost degradation on the Tibetan
790 Plateau during the 21st century. *J. Geophys. Res. Atmos.* **117**, D05106,

791 doi:10.1029/2011JD016545 (2012).

792 74. D. Lawrence, A. Slater, S. Swenson, Simulation of present-day and future
793 permafrost and seasonally frozen ground conditions in CCSM4. *J. Clim.* **25**,
794 2207–2225 (2012).

Acknowledgments. This research was jointly supported by the National Natural Science Foundation of China (42088101, 41991281 and 42275027) and CAS "Light of West China" Program (xbzg-zdsys-202102). The CESM project is supported primarily by the National Science Foundation (NSF). This material is based upon work supported by the National Center for Atmospheric Research (NCAR), which is a major facility sponsored by the NSF under cooperative agreement no. 1852977. Ran Feng acknowledges the U.S. NSF grant 1814029 and 1903650 for generating the CESM2 mPWP simulation. V. Romanovsky acknowledges the U.S. NSF grant 1832238 for supporting his involvement in this study. Gerrit Lohmann and Christian Stepanek acknowledge institutional funding via the research program PACES-II of the Helmholtz Association and by the Helmholtz Climate Initiative REKLIM.

Author Contributions. D.G. and H.W. designed the study. D.G. performed research. D.G., V.E.R., J.S., and Z.Z. analyzed data. A.M.H., U.S., Z.Z., X.L., Q.Y., B.L.O., R.F., G.L., C.S., A.A., W.C., W.R.P., D.C., A.S.v., C.C., M.A.C., N.T., Q.Z., S.J.H., and Y.K. contributed new reagents/analytic tools. D.G., N.P., and C.S. wrote the paper. All authors discussed the results and reviewed the manuscript.

Competing interests. The authors declare no competing interest.

Figure captions

Figure 1. Difference in near-surface permafrost between the mid-Pliocene warm period (mPWP) and preindustrial period (PI), simulated with the SFI model driven by corrected climate data from each PlioMIP2 model and their ensemble mean (ENS). (a) Differences in near-surface permafrost area (left, bars, %, (mPWP–PI)/PI×100) and mean annual surface air temperature (right, circles, °C, mPWP–PI) averaged over the present-day permafrost region for each model and the ENS. Error bars (blue: permafrost area, black: temperature) on the ENS bar/circle indicate one standard deviation across the 17 climate models. The dashed horizontal line represents a 100% difference in permafrost area. The standard deviation is calculated across the 17 climate models. R represents the correlation coefficient between the difference in near-surface permafrost area and the difference in mean annual temperature for each model. (b) Difference in near-surface permafrost extent in ENS. Areas outlined in red are the simulated near-surface permafrost extent during the mPWP, while areas outlined in black are the simulated near-surface permafrost extent during the PI. Shading denotes the differentiation of mPWP near-surface permafrost extents from the 17 models. The unit on the color bar is the total number of models that captured near-surface permafrost within the given area (red refers to more models and blue/purple refers to fewer models). ENS area difference is the percentage difference in ensemble mean near-surface permafrost area during the mPWP relative to the PI.

Figure 2. Mean bias (MB, °C) of simulated mean annual temperature change during the mid-Pliocene warm period (mPWP), validated against proxy data (circles on maps) (simulation minus proxy data). (A) MB of the three groups of models (group 1: –3 °C<MB<0 °C, group 2: –5 °C<MB<–3 °C, group 3: MB<–5 °C) and their ensemble mean (ENS). Error bars on ENS bars indicate one standard deviation across the models in each group. (B), (C) and (D) are spatial patterns of bias of the three model groups' ENS, with the ENS MB (all stations) given at the bottom of each panel.

Figure 3. Difference in near-surface permafrost extent between the mid-Pliocene warm period (mPWP) and preindustrial period (PI), simulated with the SFI model

driven by corrected climate data from the three model groups. (A), (B) and (C) represent group 1: –3 °C<MB<0 °C, group 2: –5 °C<MB<–3 °C and group 3: MB<–5 °C, respectively. Areas outlined in red show the model ensemble mean (ENS) near-surface permafrost extent during the mPWP, while areas outlined in gray (panel A)/black (panels B and C) illustrate the respective near-surface permafrost extent during the PI. Shading denotes the differentiation of mPWP near-surface permafrost extents derived from individual models in each group. The unit of each color bar is the total number of models that captured near-surface permafrost at that location. ENS area difference is the percentage difference in ensemble mean near-surface permafrost area during the mPWP relative to the PI. The standard deviation is calculated across all climate models within the relevant model group. In Panel (A), the sites, where mPWP permafrost reconstruction records are available, are represented with circles and rectangles. Permafrost is assumed to be absent (present) at each site marked by a circle (rectangle). LE: Lake El'gygytgyn in northeastern Arctic Russia (39); OP: Ocean Point in northwestern Alaska (32); KL: Klondike area in western Canada (40); EI: Ellesmere Island area in Canada's High Arctic (38). Note that KL and EI represent an area surrounding the site, not just the site location because the longitudes/latitudes of site KL, provided by the literature (40), appear to be regional mean coordinates, and the longitude/latitude of EI, provided by the literature (38), is only approximate.

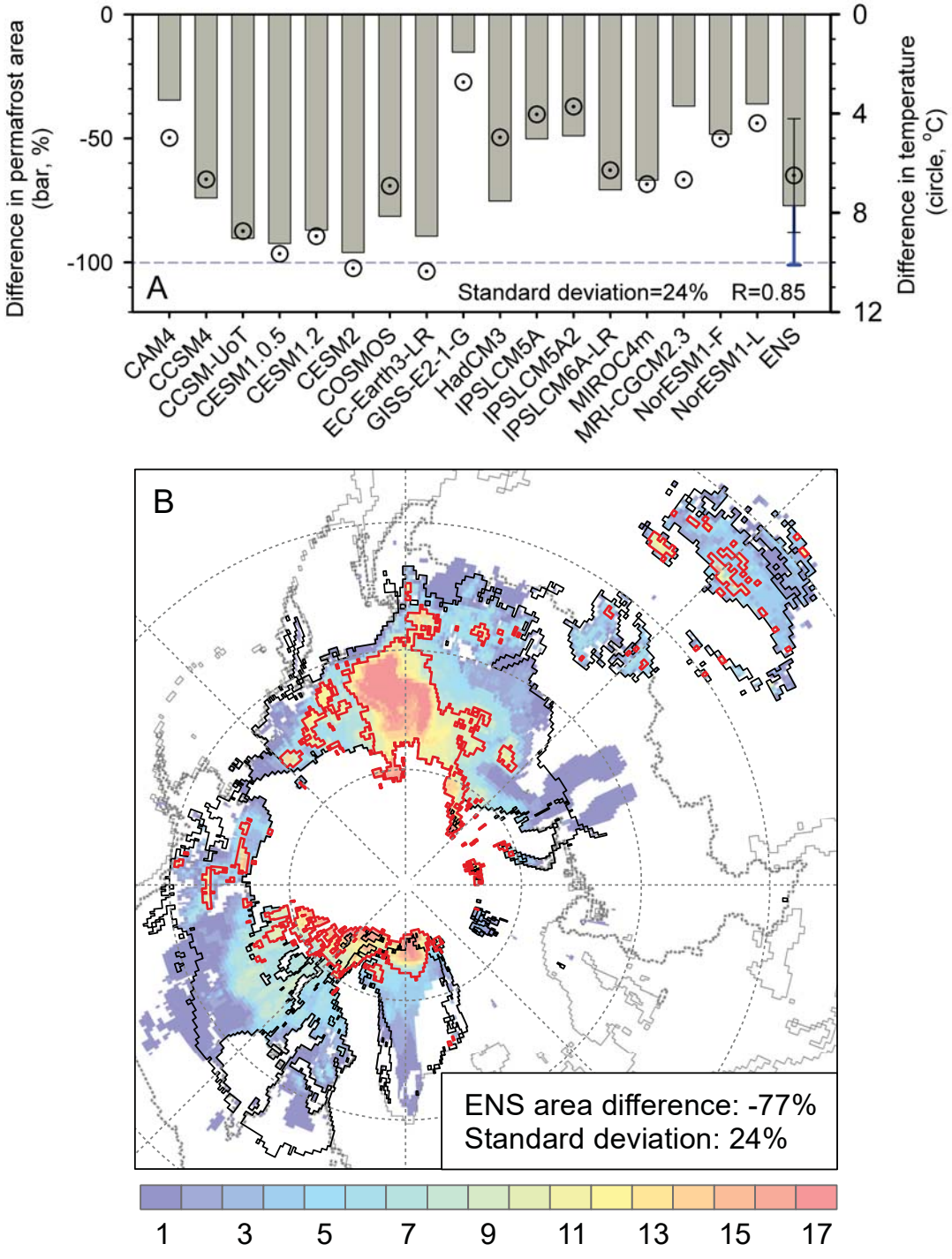
Difference in permafrost area (bar, %)
Difference in temperature (circle, °C)
0
-50
-100
0
4
8
12
A
Standard deviation=24%
R=0.85
CAM4
CCSM4
CCSM-UoT
CESM1.0.5
CESM1.2
CESM2
COSMOS
EC-Earth3-LR
GISS-E2-1-G
HadCM3
IPSLCM5A
IPSLCM5A2
IPSLCM6A-LR
MIROC4m
MRI-CGCM2.3
NorESM1-F
NorESM1-L
ENS
B
ENS area difference: -77%
Standard deviation: 24%
1
3
5
7
9
11
13
15
17

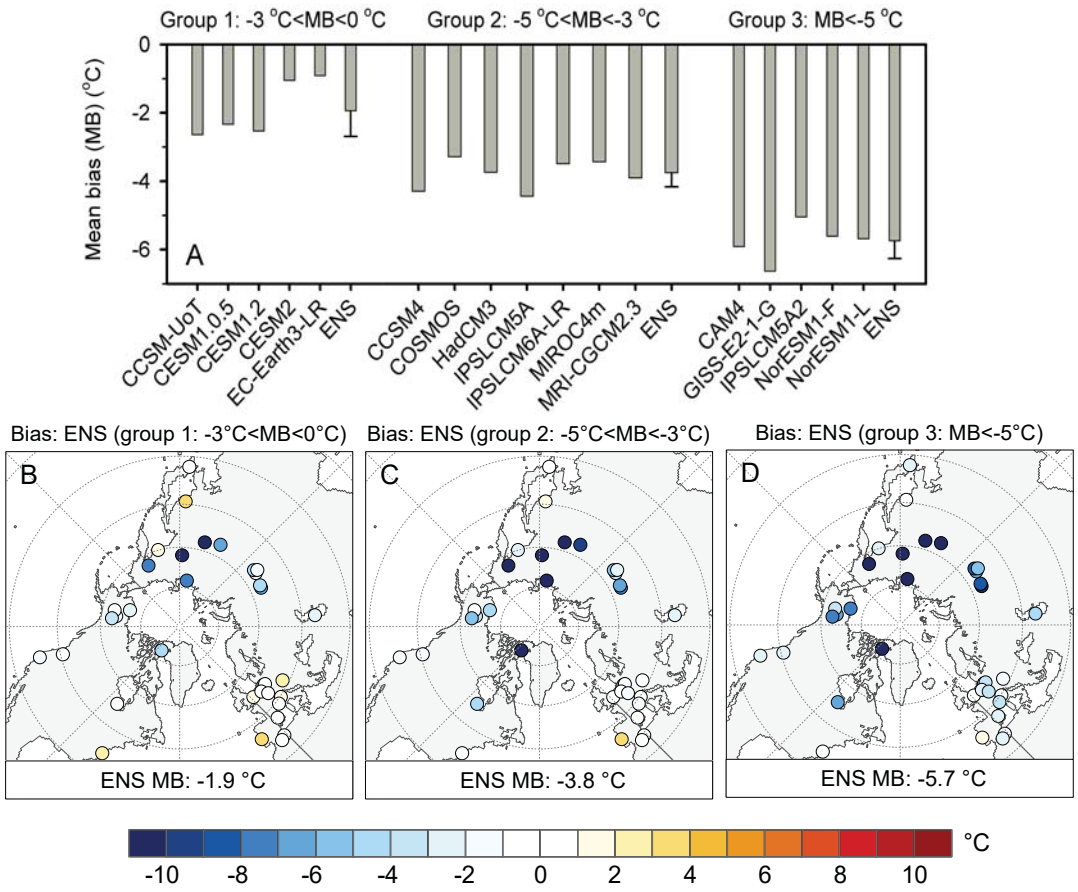
Group 1: -3 °C<MB<0 °C
Group 2: -5 °C<MB<-3 °C
Group 3: MB<-5 °C
Mean bias (MB) (°C)
0
-2
-4
-6
A
CCSM-UoT
CESM1.0.5
CESM1.2
CESM2
EC-Earth3-LR
ENS
CCSM4
COSMOS
HadCM3
IPSLCM5A
IPSLCM6A-LR
MIROC4m
MRI-CGCM2.3
ENS
CAM4
GISS-E2-1-G
IPSLCM5A2
NorESM1-F
NorESM1-L
ENS
Bias: ENS (group 1: -3°C<MB<0°C)
Bias: ENS (group 2: -5°C<MB<-3°C)
Bias: ENS (group 3: MB<-5°C)
B
C
D
ENS MB: -1.9 °C
ENS MB: -3.8 °C
ENS MB: -5.7 °C
°C
-10
-8
-6
-4
-2
0
2
4
6
8
10

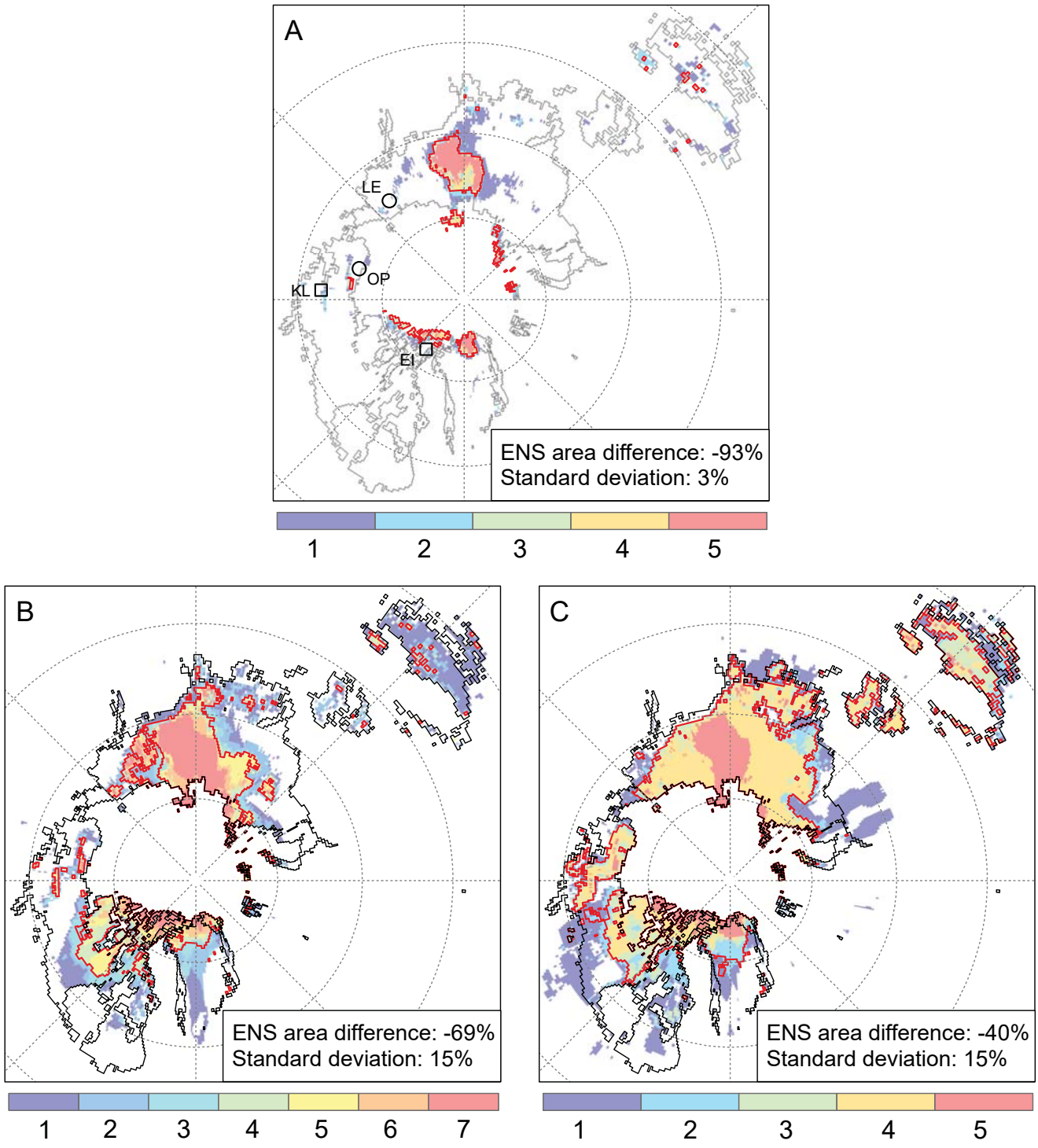
A
LE
OP
KL
EI
ENS area difference: -93%
Standard deviation: 3%
1
2
3
4
5
B
ENS area difference: -69%
Standard deviation: 15%
1
2
3
4
5
6
7
C
ENS area difference: -40%
Standard deviation: 15%
1
2
3
4
5